

Dispersion hardening using amorphous nanoparticles deployed via additive manufacturing

Received: 31 August 2024

Accepted: 2 April 2025

Published online: 15 April 2025

 Check for updates

Ge Wang^{1,9}, Yin Zhang^{2,9}, Jian Liu^{3,9}, Wen Chen³, Kang Wang¹, Bo Cui¹, Bingkun Zou¹, Qiubao Ouyang¹, Yanming Zhang⁴, Zhaoyang Hu⁴, Lu Wang⁴, Wentao Yan⁴, Shenbao Jin⁵, Jun Ding⁶, Y. Morris Wang⁷, Ting Zhu⁸, Zan Li¹✉, Di Zhang¹✉ & Evan Ma⁶✉

Nanoparticles or precipitates are long used to block dislocations to strengthen metals. However, this strengthening mechanism unavoidably adds stress concentrations at the obstacles, instigating crack initiation that hampers ductility. Here, we demonstrate a strategy that replaces the traditional crystalline dispersions with dense amorphous nanoparticles, which is made possible via laser powder bed fusion. Porosity-free copper-based nanocomposites are demonstrated as a prototype, consisting of densely and uniformly distributed amorphous boron–carbide nanoparticles (~47 nm in average diameter, up to 12% volume fraction) via an in situ nanofragmentation and melt-quench process. The amorphous nanoparticles act as dislocation sinks, thereby alleviating local stress concentration. They also self-harden along with tensile deformation, promoting strain hardening and therefore homogeneous plastic flow. The as-built composite achieves a tensile strength of more than one gigapascal and a total elongation of approximately 10%, more than twice that of its crystalline dispersion counterpart. Defect accumulation is also suppressed upon cyclic deformation of the as-built bulk nanocomposites, delivering a fatigue strength limit (at $> 10^7$ cycles) of more than 70% of the tensile strength. Our results demonstrate an effective strategy for additive manufacturing of metallic materials with superior properties.

In metallic materials, dispersing obstacles (such as hard particles and precipitates) to block moving dislocations is a commonly used approach for strengthening purposes^{1–3}. This widely adopted “dispersion hardening” mechanism, however, often sacrifices ductility, because dislocation pile-ups at the obstacles lead to stress

concentration, facilitating the nucleation of cracks^{4–6}. We propose here to replace the conventional crystalline dispersions with amorphous nanoparticles. This is a likely solution to the problem, because an amorphous phase and its interface with the matrix have been reported to act as dislocation sources and sinks^{7,8}, which would help alleviate the

¹State Key Laboratory of Metal Matrix Composites, Shanghai Jiao Tong University, Shanghai, China. ²State Key Laboratory for Turbulence and Complex System, College of Engineering, Peking University, Beijing, China. ³Department of Mechanical and Industrial Engineering, University of Massachusetts, Amherst, MA, USA. ⁴Department of Mechanical Engineering, National University of Singapore, Singapore, Singapore. ⁵School of Material Science and Engineering, Hebei University of Technology, Tianjin, China. ⁶Center for Alloy Innovation and Design, State Key Laboratory for Mechanical Behaviour of Materials, Xi'an Jiaotong University, Xi'an, China. ⁷Department of Materials Science and Engineering, University of California, Los Angeles, CA, USA. ⁸Woodruff School of Mechanical Engineering, Georgia Institute of Technology, Atlanta, Georgia, USA. ⁹These authors contributed equally: Ge Wang, Yin Zhang, Jian Liu. ✉e-mail: njulizan@sjtu.edu.cn; zhangdi@sjtu.edu.cn; maen@xjtu.edu.cn

stress concentrations at the obstacles. As such, amorphous nanoparticles would be the dispersion of choice, in delaying damage nucleation to significantly improve ductility and other damage-sensitive in-service properties such as fatigue resistance.

The question is then how to realize a dense and uniform dispersion of amorphous nanoparticles inside the metals. To this end, we take advantage of additive manufacturing (AM)^{9–11}. This non-equilibrium processing route and associated complex melt flow have been known to provide opportunities for tailoring the microstructure, including the grain morphology, subgrain dislocation structure and chemical segregation, leading to vastly improved mechanical properties over those from traditional processing⁹. For example, we recently showed that laser powder bed fusion (L-PBF) can achieve spontaneous and intragranular dispersion of microparticles in conventional composite systems¹². Herein, we exploit L-PBF to create a new type of nanocomposite consisting of a metal matrix with uniformly and densely distributed reinforcing amorphous nanoparticles. An in situ nano-fragmentation process is exploited to spontaneously refine the crystalline reinforcing microparticles into amorphous nanoparticles during L-PBF (Fig. 1a). For the reinforcing phase, we set three criteria for the materials selection: (1) high strength and elastic modulus to ensure the desired strengthening; (2) a melting point within a control window (~3000 K) that is accessible to the L-PBF process, such that the dispersions can be turned amorphous via melting, which are then torn apart during turbulent fluid flow and rapidly quenched; and (3) no chemical decomposition or extensive reaction with the matrix pool during the melting of reinforcements¹³. We integrate Thermo-Calc software with the latest substance database to evaluate the thermally stable phases of different metal–ceramic particle systems. The above criteria led us to a system of simple boron carbide (B₄C) reinforced copper as the first model. We demonstrate in the following that L-PBF produces a high density of amorphous nanoparticles that are embedded within pure copper grains.

Results

Microstructures and their formation mechanism

High-purity copper powders (average size of ~35 μm) were mixed with crystalline B₄C microparticles (average size of ~4 μm, 12 vol.%). A porosity-free bulk composite (density: >99.8%) was then built using L-PBF (Methods). Notably, the B₄C microparticles were melted and transformed into nanoparticles with an average size of ~47 nm (see Supplementary Fig. 1a for particle size distributions), which are densely and uniformly dispersed in the copper matrix (Fig. 1b). These nanoparticles are amorphous, as indicated by the X-ray diffraction (XRD) pattern and nuclear magnetic resonance (NMR) spectrum (Supplementary Fig. 1b, c)¹⁴. Electron backscatter diffraction (EBSD) imaging of the cross-sectional regions indicates that the copper grains are equiaxed, with ultrafine grains averaging to 0.39 ± 0.14 μm (Fig. 1b). High-resolution transmission electron microscopy (HRTEM) indicates the presence of nanocrystals (black regions, sizes of ~2.9 nm) inside the amorphous nanoparticles (Fig. 1c, d). Observing along the [110] face-centred cubic (FCC) zone axis via high-angle annular dark-field (HAADF) scanning transmission electron microscopy (STEM), we find that the lattice spacings of these nanocrystals correspond to copper (Fig. 1e), which was confirmed by energy-dispersive X-ray spectroscopy (EDS) spectrum. Therefore, these fragmented nanoparticles are “quasi-amorphous”. We used atom probe tomography (APT) to study the nanoscale compositions of the amorphous nanoparticles and the atomic diffusion across the interface (Fig. 1f–h). The nanoparticle composition (B_{3.89}C) is close to B₄C, with 8 at% copper incorporated. Figure 1h indicates very limited diffusion of the B and C atoms into copper (~5 nm). This is because B–C has strong chemical affinity such that their robust atomic bonding did not allow the diffusion of individual elements even under molten conditions, as indicated by our ab initial molecular dynamics calculations of the

formation enthalpy of B₄C at various temperatures (Supplementary Fig. 2). On the other hand, copper atoms diffuse into the B₄C nanoparticles, forming the nanoscale clusters seen under TEM. Near-edge X-ray absorption fine-structure (NEXAFS) spectroscopy of the extracted nanoparticles (Fig. 1i) shows broadened π* peak with a relatively low intensity, which can be attributed to the amorphous structure^{15,16}. Thus, amorphous nanoparticles are generated by melting and fragmentation of the B₄C microparticles upon laser scanning, followed by rapid quenching, which kinetically inhibits the thermodynamically favoured crystallization.

The in situ nano-fragmentation of ceramic particles was achieved by increasing the input energy density of the L-PBF. We find that microparticles are retained at low energy density (86.9 J/m³) but fragmented as the energy input increased, eventually into nanoscale particles at 180.6 J/m³ (Fig. 2a). Importantly, the fast Fourier transform (FFT) images demonstrate that most of the produced fine particles are amorphous upon rapid solidification. To reveal the particle melting and fragmentation dynamics, we conducted high-fidelity simulations to track the changes in B₄C microparticles, which produced three-dimensional data at nanoscale and meso-nanosecond time resolutions (Methods). As shown in Fig. 2b–d, we observe the following microstructural changes during a single-track scan. Initially, a laser impinging on the composite powder bed increases the local temperature to a maximum value of 3800 K, directly melting the B₄C microparticles. Then, the strong and complex fluid flow induced by the large thermal gradient of L-PBF (reaching 10⁸ K/m, Supplementary Fig. 3) tears the ceramic droplets apart, gradually turning them into very fine droplets that are tens of nanometres in size (Fig. 2e). Notably, the above fragmentation process operates on the first track when the laser directly irradiates the microparticles. The subsequent laser tracks do not raise the melt pool temperature to reach the melting point of B₄C. Eventually, the Marangoni convection-induced intermixing of solidified amorphous nanoparticles with copper melt prevents particle agglomeration¹², which facilitates the observed high dispersion uniformity. The same melt-quench and fragmentation is expected to happen in other metal-ceramic particle systems to obtain similar composite structures. For example, we have achieved B₄C amorphous nanoparticles in pure aluminium using the same in situ nano-fragmentation strategy (Fig. 2f). We have also confirmed the generality in other ceramic–copper systems (e.g., CrB₂–copper nanocomposites, Fig. 2g). In all cases, the ceramic particles are fragmented to the nanoscale without marked changes in their compositions.

Tensile properties and the elimination of printing defects

We employed tensile tests to investigate the mechanical properties of the L-PBF nanocomposites. Figure 3a shows the representative tensile responses of the as-printed copper reinforced with three volume fractions (12%, 8% and 4%) of the amorphous nanoparticles (ANPs) (hereafter referred to as Cu–ANP). Copper grains show no obvious texture in the as-built samples, and their sizes decrease from 7.17 ± 4.48 μm to 0.39 ± 0.14 μm (Supplementary Fig. 4a) with increasing particle volume fraction inside. A tensile curve for conventional high-strength pure copper with a grain size (~400 nm, Methods) similar to that of Cu–12%–ANP is presented for comparison. Clearly, Cu–ANPs show much better tensile strengths and strain hardening beyond plastic yielding, leading to high ductility. Specifically, Cu–12%–ANP exhibits very high yield and tensile strengths of 729 ± 27 and 1036 ± 35 MPa, respectively, along with relatively large uniform and total elongations of $7.2\% \pm 0.4\%$ and $9.7\% \pm 0.4\%$, respectively. This enhanced tensile ductility of Cu–ANPs is further evidenced by the improvement in true fracture strain, estimated from the reduction in area at fracture (Supplementary Fig. 5). Previous AM attempts have also achieved excellent mechanical properties in other types of advanced alloys, such as titanium-based alloys, high-strength steels and high-entropy alloys; on a normalized

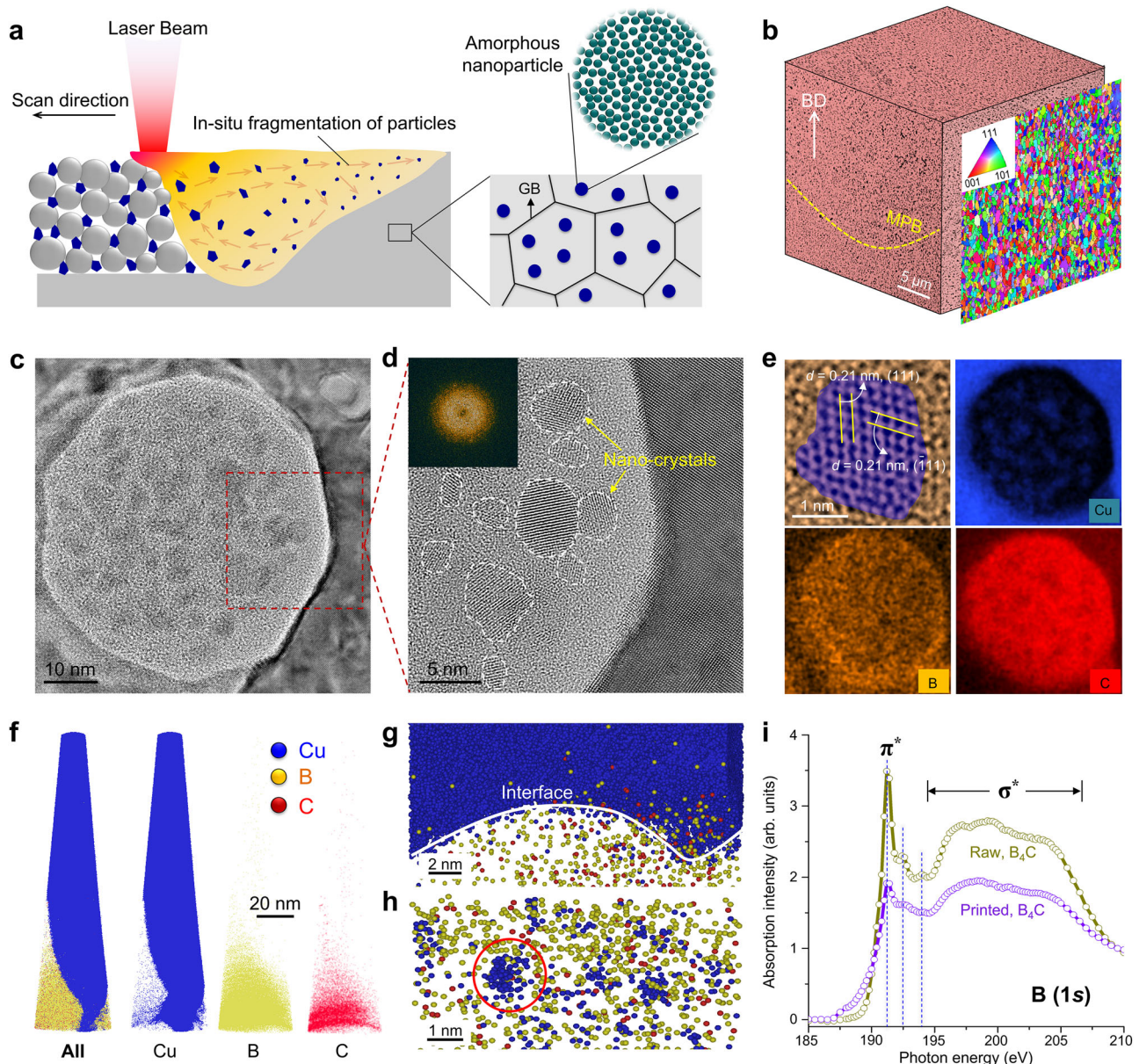


Fig. 1 | Design principles and microstructures of nanocomposites by laser powder-bed-fusion (L-PBF). **a** Schematic illustrating the manipulation of reinforcing particle structures via additive manufacturing (AM). An in situ nano-fragmentation process is utilized to spontaneously refine crystalline reinforcing microparticles into amorphous nanoparticles during L-PBF. This process involves the melting, nano-fragmentation, and rapid solidification of the reinforcing particles. GB denotes grain boundary. **b** Three-dimensional reconstructed scanning electron microscopy (SEM) images of the as-built composite. A cross-sectional electron backscatter diffraction (EBSD) image is superimposed to show the equiaxed grain structure. Melt pool boundaries (MPBs) and build direction (BD) are illustrated by the yellow dashed line and white arrow, respectively. **c** Aberration-corrected high-resolution transmission electron microscopy (HRTEM) image of a representative nanoparticle, with ultranano black regions distributed within the amorphous nanoparticles. At least twenty nanoparticles were characterized for

microstructural identification. **d** Enlarged view of the selected region in (c). The inset shows a fast Fourier transform (FFT) image of a region in the nanoparticle that does not contain Cu nanocrystals, suggesting an amorphous nature. **e** high-angle annular dark-field scanning transmission electron microscopy (HAADF-STEM) image of a tiny nanocrystal along the [110] FCC zone axis and energy-dispersive X-ray spectroscopy (EDS) images of Cu, B and C atoms. **f** Three-dimensional atomic probe tomography (APT) reconstructions of Cu, B and C atom distributions in a typical APT tip including a matrix Cu–nanoparticle interface. The Cu, B and C atoms are coloured blue, yellow and red, respectively. **g, h** Measured distributions of the three atomic species near the interface and inside the nanoparticle, respectively. The phase boundary (PB) is indicated by the white line, and a representative tiny Cu cluster/nanocrystal is highlighted by a red circle. **i** Near-edge X-ray absorption fine-structure (NEXAFS) spectrum at the B–K edges of the extracted nanoparticles from the as-built composite.

basis, the properties of our L-PBF nanocomposites are even better than those state-of-the-art AM materials (Fig. 3b, see Supplementary Note 1 for the symbol description and associated reference details). Our copper nanocomposites also demonstrate strength–ductility combinations that surpass previous types of copper-based alloys and are comparable to the well-known high-strength copper-beryllium alloy (noting that beryllium is toxic) (Fig. 3c; see

Supplementary Note 2 for referential data). It is worth mentioning that ANP-reinforced pure copper is used here to demonstrate the basic principle of dispersion hardening with amorphous nanoparticles. Nanocomposites with unprecedented mechanical properties are highly anticipated when this strategy is applied to typical high-strength copper alloys. To see the advantage of ANPs, we also annealed the as-built samples at 1173 K for 6 h, after which the

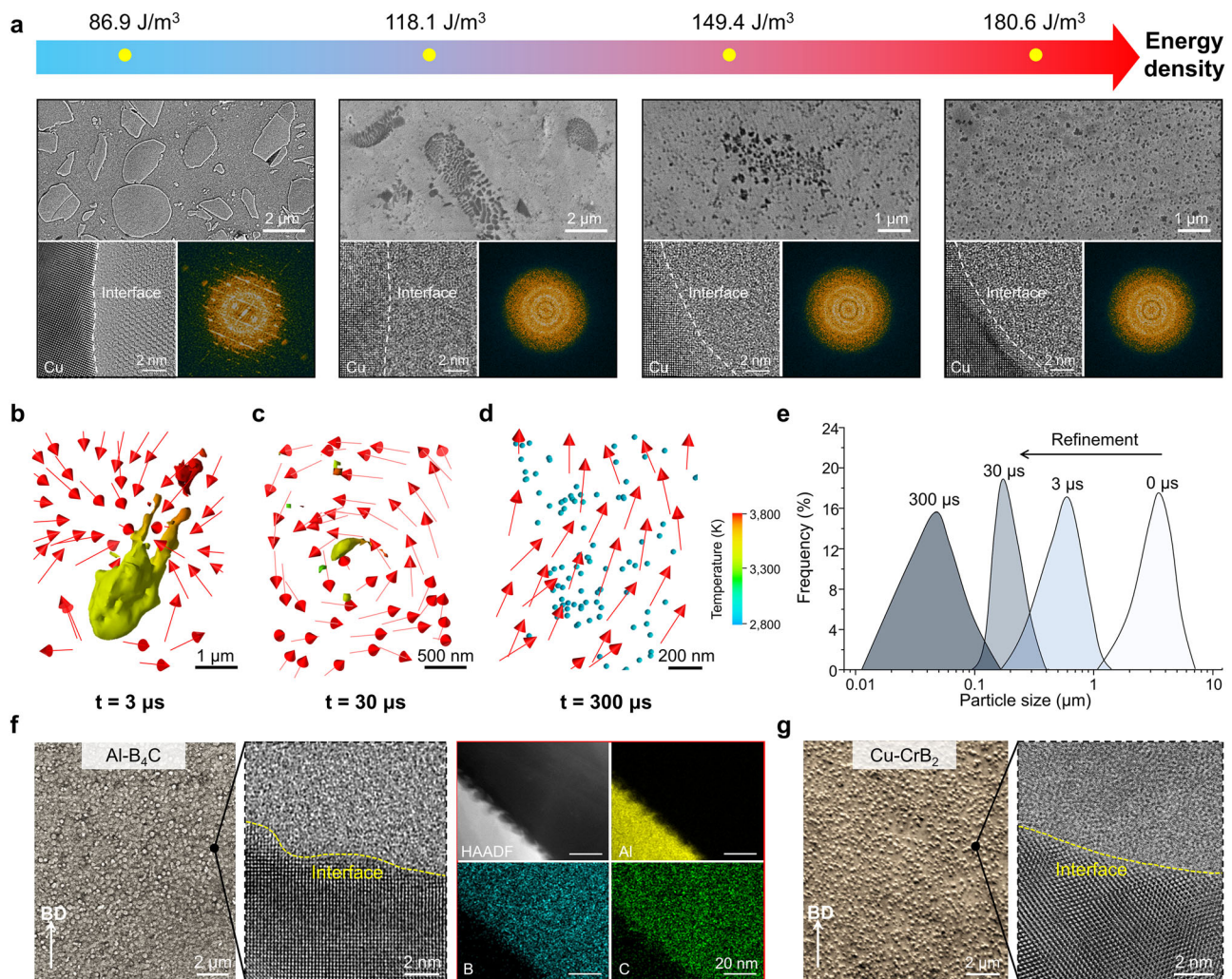


Fig. 2 | Nanofragmentation mechanism of microparticles. **a** Changes in the morphologies of reinforcing particles as a function of the input volumetric energy density, E_d . ($E_d = P/vhd$, where P is the laser power, v is the scan speed, h is the hatch distance, and d is the layer thickness). A representative HRTEM image of the interface and the corresponding FFT image of a region in the refined particle, displayed for samples processed with different E_d . The volume fraction of B_4C is 12% in all samples. Images at different locations (at least five) show similar morphologies with the representative ones. Note that most of the refined particles (with an E_d value larger than 118.1 J/m^3) have amorphous structures, thereby suggesting the melting–fragmentation–solidification process of B_4C microparticles upon L-PBF. **b–d** High-fidelity multiphysics modelling of the change in the particle morphology during L-PBF. The coloured arrows represent the velocity vector in the melt, under which the initially micro-sized ($\sim 4 \mu\text{m}$ in diameter) particle is gradually fractured into nanoparticles. The particles are coloured based on their local

temperatures. **e** Statistical calculation of the particle size distribution as a function of scanning time, as obtained from the simulation results. **f** SEM image of the as-built $Al-B_4C$ composites and HAADF-STEM image of interfacial structure of the selected region, showing the same in-situ nanofragmentation behaviour as in Cu, now forming ANPs with sizes $\sim 200 \text{ nm}$. BD stands for build direction. Beam direction is along the $[100]$ zone axis of aluminium. EDS mapping indicates that the composition of the nanoparticle is $78.7 \pm 3.5 \text{ at\%}$ of B, $18.8 \pm 3.6 \text{ at\%}$ of C and $2.5 \pm 0.7 \text{ at\%}$ of Al, with little elemental diffusion or reaction at the interface. **g** The representative SEM image and HAADF-STEM image of as-built $Cu-CrB_2$ composites. Micron-sized CrB_2 with diameters of $\sim 10 \mu\text{m}$ were used as the starting reinforcing particles, which have been spontaneously turned into amorphous nanoparticles with sizes of $\sim 40 \text{ nm}$. Beam direction is along the $[110]$ zone axis of copper. At least five different locations were independently observed for microstructures shown in (**f** and **g**) showing similar results.

amorphous B_4C became crystallized nanoparticles (CNPs) (referred to as Cu–CNPs) (Supplementary Fig. 4b). Because of the strong pinning of grain growth by the nanoparticles, the grain size of the annealed nanocomposite remained almost unchanged (Supplementary Fig. 4c). Cu-12%–CNP shows a tensile elongation of only $\sim 3\%$, followed by sudden failure. The superiority of ANP in tuning mechanical properties is primarily manifested in its ability to enhance strain hardening, as shown by the Kocks–Mecking hardening rate plot and the increased strain hardening exponent based on the Hollomon equation (Supplementary Fig. 6a–c). As a result, Cu–ANP exhibits twice the total elongation of Cu–CNP with the same nanoparticle content.

We now discuss the several noteworthy attributes of our AM Cu–ANP composite. First of all, the complete elimination of printing defects (such as microvoids) due to inadequate fusion, is difficult for L-PBF copper-based materials because of their low laser absorptivity in the infrared laser range^{13,17,18}. We measured the laser absorptivity of our initial Cu– B_4C powder mixtures with different microparticle fractions, revealing a surprisingly high laser absorptivity of more than 70% for composite powders (8 and 12 vol.%) at a wavelength of 1064 nm (Supplementary Fig. 7a). This represents a nearly fourfold improvement in absorptivity compared to pure copper. The mechanisms of microparticles in mediating the laser–powder interaction can be revealed by using computational full laser ray tracing (Methods). The

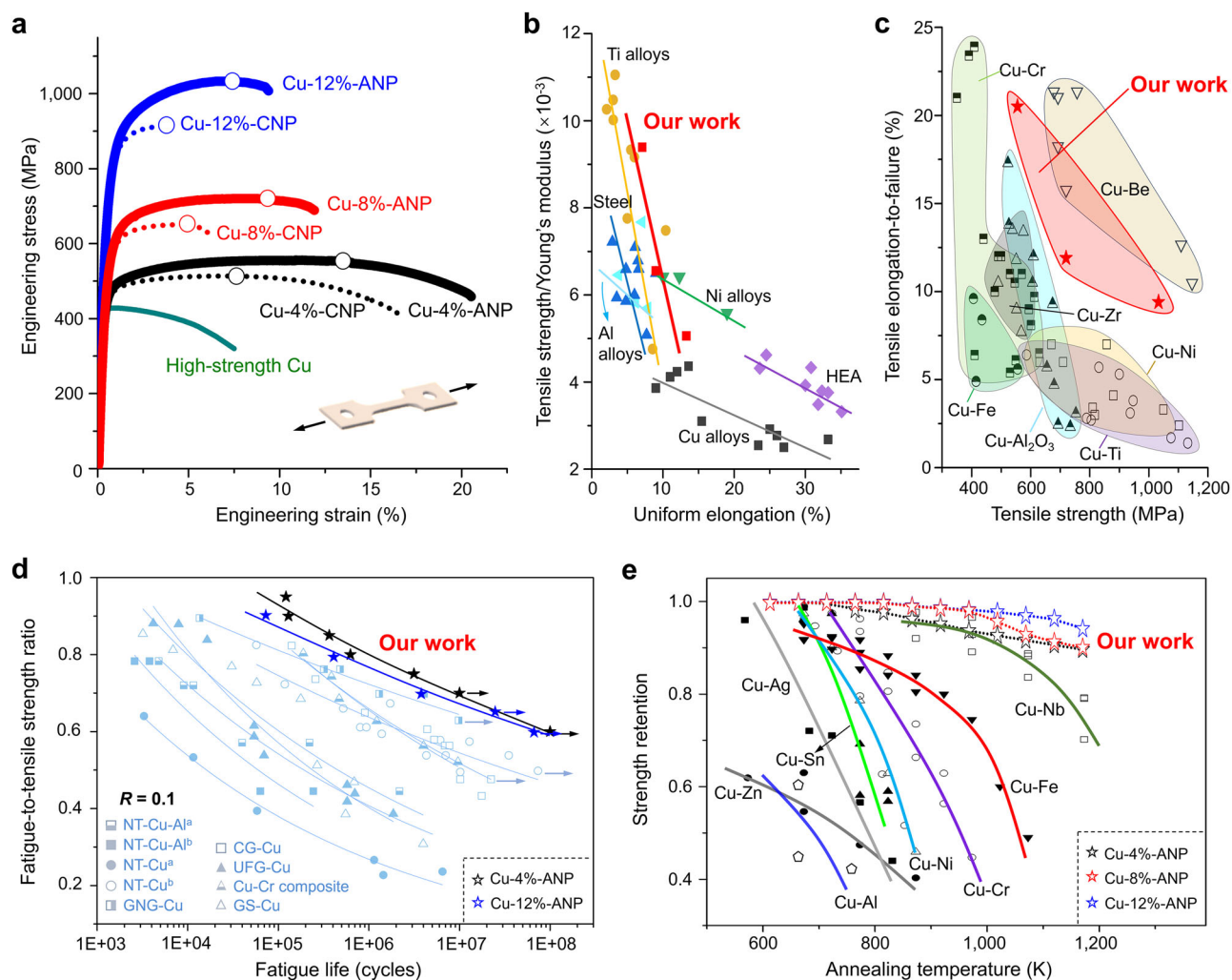


Fig. 3 | Mechanical and functional properties of the laser powder-bed-fusion copper nanocomposites. **a** Tensile stress–strain curves of the as-printed Cu-B₄C nanocomposites with different volume fractions of B₄C (12%, 8% and 4%). The as-built nanocomposites with amorphous nanoparticles are referred to as Cu-ANP. The ultimate tensile strength at which unstable deformation (i.e., necking) occurs is marked on each curve. The inset shows a schematic of a dog-bone-shaped tension specimen. A tensile curve (green) for conventional high-strength cold-rolled pure copper with a similar grain size to that of Cu-12%-ANP (i.e., ~400 nm) is presented. **b** Mechanical property comparison of our as-built copper nanocomposites with that of previous copper alloys. The referential literature data are provided in Supplementary Note 1. **c** Tensile strength versus uniform elongation of AM copper nanocomposites compared with those of representative high-performance AM metal alloys in the literature, including aluminium (Al)-based alloys, high-strength

steels, titanium (Ti)-based alloys, high-entropy alloys (HEAs) and Cu-based alloys. For fair comparisons of different metallic materials, the tensile strength is normalized by the Young's modulus. The symbol descriptions and associated references can be found in Supplementary Note 2. **d** Fatigue life (the number of cycles to failure) against the fatigue strength-to-tensile strength ratio of the Cu-4%-ANP and Cu-12%-ANP nanocomposites, along with references for the reported state-of-the-art copper materials, including nanograin, gradient and nanotwinned microstructures. The fatigue properties of the well-annealed coarse-grained copper are shown. Each comparison sample has a stress ratio *R* of 0.1. The symbol description and associated references can be found in Supplementary Note 4. **e** Strength (hardness) retention of our L-PBF Cu-ANP after annealing at different temperatures for 1 h compared with that of conventional copper-based alloys (see Supplementary Note 5 for more reference information).

majority of laser rays, which penetrate the powder via multiple reflections, are found to be eventually absorbed by the microparticles as a result of their significantly higher absorptivity compared to copper powders (Supplementary Fig. 7b–d). This prevents powder spattering and localized laser heating in the composite powder bed, promoting a uniform energy absorption process¹⁹. Moreover, previous reports indicate that the particle-induced increase in melt viscosity can stabilize vapor depression fluctuations and control liquid droplet coalescence^{20,21}, enabling a dramatic reduction of defects. Due to these effects, the relative density of all our as-built samples is as high as >99.8%. Such an improvement of microstructural consistency and the elimination of printing porosities would help the nanocomposites to fully display their intrinsic mechanical properties.

Strengthening and stress delocalization behaviour

The high yield strength of our as-built copper nanocomposites can be explained by the Orowan strengthening mechanism due to densely distributed nanoparticles, aided also by the high densities of dislocations and grain refinement introduced during L-PBF, as revealed by our strengthening mechanism analyses in Methods subsection 'Estimating the yield strength of the as-built nanocomposites'. Traditionally, dislocations bypassing obstacles could accumulate in the form of Orowan loops²². The microstructural heterogeneity adds long-range back stresses on the ensuing dislocations to promote hardening. However, the dislocations stored would normally cause interface stress concentrations and crack nucleation, leading to reduced ductility. Our Cu-ANP does not face this traditional dilemma, such that the ductility

is much improved. This is evidenced by the findings via fracture surface analyses. Notably, Cu-12%-ANP shows no evidence of nanoparticles in the dimples, in contrast to the corresponding Cu-12%-CNPs, which contain many nanoparticles at the bottoms of their dimples (Supplementary Fig. 8a, b). This observation indicates that the CNPs led to stress concentrations at interphase interfaces and tend to nucleate cracks/decohesion upon deformation, similar to the failure behaviours of precipitate-strengthened alloys²². In stark contrast, amorphous nanoparticles do not suffer from this drawback. The absence of premature failure in Cu-ANP nanocomposites is consistent with the presence of necking, as predicted by the Considère criterion (see Supplementary Fig. 6d); however, the Cu-12%-CNP nanocomposite fractures before necking occurs, indicating significant stress concentration. As shown in Fig. 4a, a group of grains after 3% strain is examined using high-resolution EBSD, which enables a quantitative cross-correlation-based analysis of strain and stress (Methods). As observed, the residual elastic strain field relative to the reference region (i.e., the lowest kernel average misorientation value within a grain) in the Cu-ANP sample exhibits much lower magnitudes and more uniform distributions across all selected grains, compared with its crystallized counterpart. For a further precise evaluation of the deformation compatibility in Cu-ANP, we conducted precession electron diffraction (PED)-based automated crystal orientation mapping (ACOM) via TEM for the 3%-deformed sample, with a mapping spatial resolution of 1 nm (Fig. 4b). Specifically, the two-beam bright-field TEM images show random distributions of dislocations inside the copper grains, and no discernible dislocation pile-ups are observed at the matrix-nanoparticle interface. The overall dislocation density, as estimated from the TEM images of the deformed Cu-ANP, is higher ($-1.1 \times 10^{15} \text{ m}^{-2}$) than that in the as-printed state ($-2.3 \times 10^{14} \text{ m}^{-2}$), suggesting dislocation multiplication and therefore strain hardening. Note that the point-to-point misorientation profile reveals a very low local misorientation across the interface (less than 0.5° , Fig. 4b), indicating a more uniform spread of the stored dislocations. It appears that the geometrically necessary dislocations that would otherwise pile-up near the interfaces have been accommodated via shear transformations at the surface of the ANPs (to be discussed below). On the contrary, in the CNP case dislocations piled up as expected, to accumulate at the Cu-CNP interface, as evidenced by both the post-deformation TEM and electron channelling contrast imaging analyses (Supplementary Fig. 9). This ANP-induced stress delocalization at the interface is the primary mechanism driving stable deformation without premature failure in the L-PBF nanocomposites.

In situ synchrotron XRD and atomic scale modelling

We also employed in situ synchrotron XRD experiments with crystal plasticity finite element (CPFE) modelling (Methods)⁹. This approach allows us to dissect the mechanical behaviour of each sample component despite the amorphous nature of the nanoparticles. Figure 4c shows the lattice strain ϵ_{hkl} along the loading direction against the applied true stress (σ) for several representative $\{\text{hkl}\}$ reflections of copper in different nanocomposites (hollow symbols, 8 vol.% of nanoparticles). Initially, all reflections exhibit elastic deformation, with slopes differing due to the elastic anisotropy of diffraction planes. Upon straining, the lattice strain of the $\{220\}$ reflection in both samples first shows a nonlinear trend, turning upwards, and the lattice strain of the $\{200\}$ reflection deviates from a linear trend in a downward direction due to the occurrence of load transfer from the soft $\{220\}$ to hard $\{200\}$ reflections, revealing the early onset of microplastic yielding. As deformation proceeds, progressive yielding occurs sequentially from the $\{111\}$, $\{311\}$ to $\{200\}$ reflections. Notably, compared with those of Cu-CNPs, the crystallographic families of Cu-ANPs are more resistant to softening due to the greater uniform elongation values of the composites. We calibrate our CPFE model in terms of simulated lattice strain responses based on in situ diffraction data (solid lines in Fig. 4c).

The stress-strain curves derived from the CPFE model closely match the experimental data (Supplementary Fig. 10a). Then, we inversely determine the constitutive relationships between copper and nanoparticles as a function of applied strain during deformation, the results of which are displayed in Fig. 4d. Copper in Cu-ANP has a lower initial yield strength due to the lower initial dislocation density (Supplementary Fig. 10b); a higher dislocation density in Cu-CNP may be attributed to thermal misfit upon sample cooling after heat treatment²³; however, its dislocation accumulation and strain hardening rates are slightly greater. Importantly, the ANPs demonstrate remarkably improved strain hardening, contributing to most (61%) of the strain hardening magnitude of Cu-ANP (the true strain ranges from 1% to 7%). This significantly improved hardening is primarily attributed to the self-hardening (and stiffening) of the ANPs as well as the associated hardening of the interface-affected zone²⁴. Here, the ANPs have been rapidly melt-quenched at cooling rates around 10^8 K/s , such that many dangling bonds and much excess volume would be available for bond switching to accomplish shear transformations²⁵. This latter process accommodates the dislocations running into the nanoparticles, and relieves the strain incompatibility across the metal-nanoparticle interface. Hence, ANPs can play a dual role in the tensile properties of the L-PBF nanocomposites. They themselves dynamically work harden while simultaneously eliminating excessive dislocation loops and stress concentrations at the interfaces. In addition, the dislocation segments that interact locally with ANP at the interface undergo a thermally activated process with small activation volumes. This behaviour is reflected in multiple stress relaxation tests, which revealed a physical activation volume (V) of $\sim 20 b^3$ for the representative Cu-8%-ANP nanocomposite (Supplementary Fig. 11). This value is comparable to, or even smaller than, those reported in nano-grained metals (on the order of tens of b^3), highlighting the unique dislocation manipulation behaviour induced by ANPs.

Atomic scale information lends support to the above mechanisms in our Cu-ANPs. Recent studies have shown that the nanosized amorphous phases in crystal-glass composites can act as high-capacity sinks for dislocations^{26–28}, enabling the absorption of excess energy transported by the dislocations. In our molecular dynamics (MD) simulations, we do not observe any dislocation loops storing at the ANPs after the dislocation bypassing (Fig. 4e), suggesting their absorption by the ANPs along with straining. This is a key difference from the stress concentration at the usual crystalline dislocation obstacles. Moreover, the elastic strain field induced by incoming dislocations and the residual interfacial stress after the previous dislocation bypass is also relieved by the emission of dislocations on a different slip plane from the ANP interface (Supplementary Movie S1). As a result, the local nonhomogeneous deformation at the interfaces and the loops after dislocation bypassing can be effectively accommodated in the Cu-ANP nanocomposites, leaving minimal stress concentrations at the interfaces (Fig. 4e, right panel). The accommodating ability of the rapidly quenched amorphous nanoparticles is noteworthy: the pre-existing excess volume within the particles would enhance the atomic shuffling events (collective atomic rearrangements are known as shear transformations via bond switching) to accommodate the incoming dislocations and local strain^{7,27}. In other words, the local structural configurations inside the ANPs evolve during straining, and the associated bond breaking and reforming (with other neighbours) help to relieve stress concentrations at metal-ANP interfaces. This is consistent with the dynamic evolution of local strains in the ANP (Supplementary Movie S2) and the nonuniform distribution of the von Mises equivalent strain at the moment of dislocation bypassing (Fig. 4f). The high cooling rate of up to 10^8 K/s during L-PBF endows the formed ANPs a highly rejuvenated state with a high potential energy. Such a rejuvenated state contains many fertile sites for bond-switching shear transformations under loading, and also for subsequent structural relaxation to relatively low energy states. The

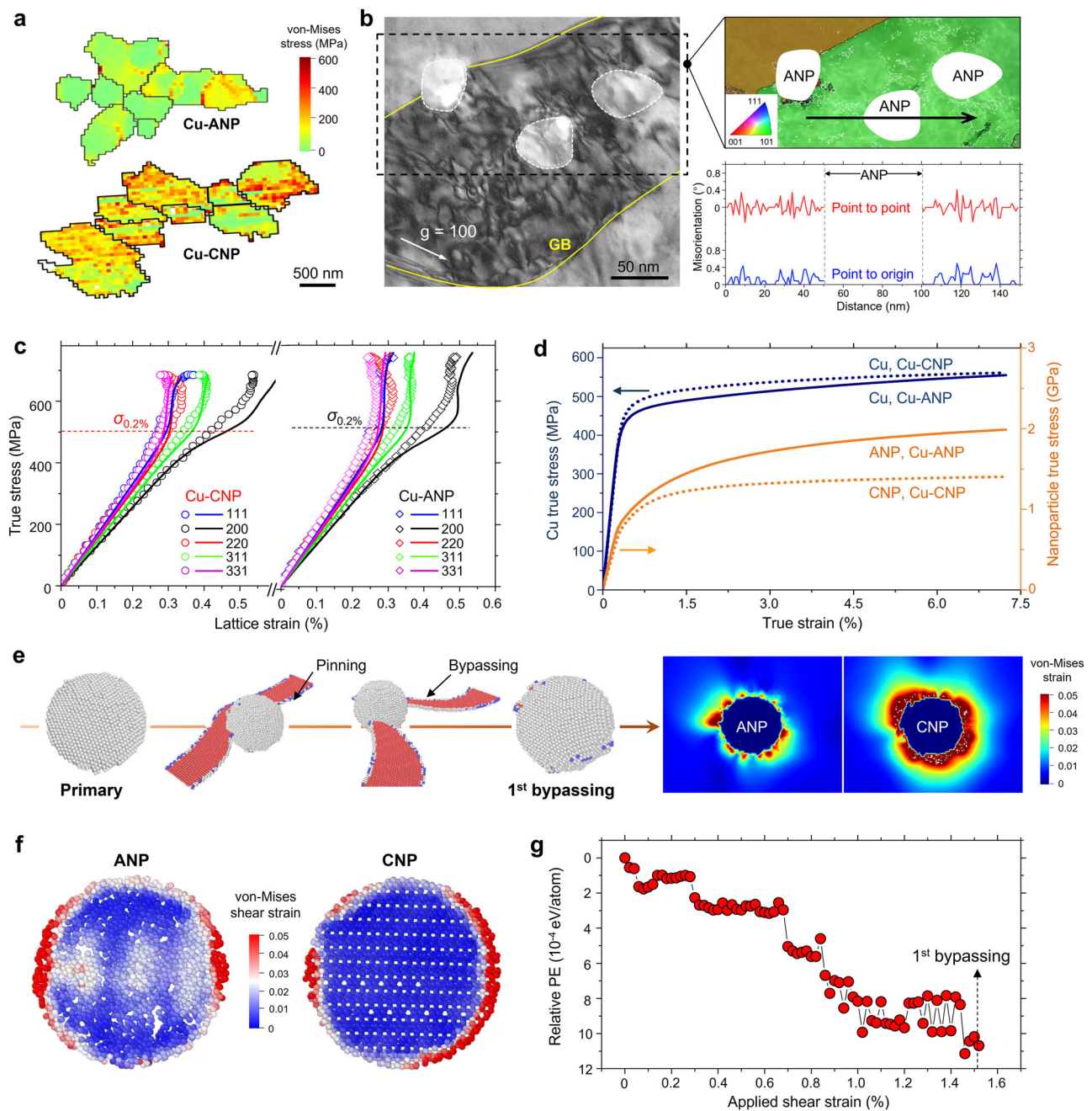


Fig. 4 | Deformation mechanism in laser powder-bed-fusion copper nanocomposites. **a** Strain mapping analysis of grains in Cu-12%-ANP and Cu-12%-CNP nanocomposites after tensile strain of 3%, as obtained from high-resolution EBSD (HR-EBSD) images. CNP refers to a crystallized nanoparticle. The zero-stress reference point is chosen as the position with the lowest kernel average misorientation (KAM). **b** Representative two-beam bright-field TEM image of the deformed Cu-12%-ANP nanocomposites (3% strain). The right column shows the inverse pole figure (IPF; top panel) map of the selected region, with the associated image quality map superimposed. The data are acquired using precession electron diffraction (PED)-based automated crystal orientation mapping (ACOM) in a TEM with a step size of 1 nm. Three experiments were repeated independently and get the similar results. Plots of the variation in the misorientation angle, measured with respect to the origin and from point to point, across the representative ANP after deformation, indicated by the solid black line in the IPF map. **c** Changes in the lattice strains in Cu-8%-ANP and Cu-8%-CNP nanocomposites against macroscopic

true stress for representative FCC (including {111}, {200}, {220}, {311} and {222}) crystallographic plane families along the loading direction. The experimental and crystal plasticity finite element (CPFE) modelling results are represented by symbols and solid lines, respectively. The macroscopic yield strengths of the different samples are marked with dashed lines. **d** CPFE simulation results of the macroscopic stress-strain responses with the corresponding stress partitioning in the copper matrix and nanoparticles. **e** Snapshots of the forward-moving dislocation interacting with the primary ANP, as observed in molecular dynamics (MD) simulations. The corresponding maps showing the atomic von Mises strain in copper are displayed in the right panels. **f** Corresponding von Mises shear strain maps in the ANP and CNP after dislocation bypassing. The whole deformation process of nanoparticles in different samples can be seen in Supplementary Movies S2 (for ANP) and S3 (for CNP). **g** Changes in the relative potential energies of atoms in the ANP (energy change relative to its original state) as functions of applied shear strain.

easier-to-activate fertile sites get gradually consumed with increasing straining, making the ANP more and more load bearing²⁹. This is supported by the observed continuous decreases in configurational potential energy with applied strain in our MD simulations (Fig. 4g), as well as the reduced strain hardening rate in a partially relaxed sample via annealing (Supplementary Fig. 8c, d). Previously, amorphous phases have been incorporated in metallic systems, such as in copper and intermetallic-based alloys^{7,30,31}. However, those studies are limited to thin-film samples, which contain amorphous phases in the form of two-dimensional laminates or three-dimensional continuous networks, rather than nano-dispersions in bulk alloys. We further note that the copper nanocrystals in ANPs could play an insignificant role in the deformation mechanisms (see additional discussion in Supplementary Note 3 for more details).

Exceptional fatigue resistance and other properties

Our reduced propensity for damage initiation/accumulation at interfaces may also render exceptional fatigue resistance. This is found to be true, as demonstrated in Supplementary Fig. 12a. Both the ascending and descending branches of the hysteresis loops of Cu-ANP (4% B₄C as a representative) overlap completely throughout the cyclic loading process, even after 10⁷ cycles at a maximum stress of 70% of its tensile strength. This stable cyclic deformation is distinct from the strain localization and cyclic hardening characteristics of alloys or conventional metal composites^{32,33}. The fatigue strength limit is greater than 70% of the tensile strength, surpassing that of state-of-the-art copper materials, including nanograined, gradient and nanotwinned copper (Fig. 3d), see Supplementary Note 4. Other properties of interest, which have also been much improved, include the electrical conductivity and thermal stability. Precipitates in alloys at high number densities (10²⁰–10²⁴/m³)³⁴ usually scatter electrons and reduce electrical conductivity. Also, these precipitates suffer from diffusion-controlled coarsening (i.e., Ostwald ripening) and are microstructurally unstable at high temperatures³⁵. As indicated in Fig. 3e, the L-PBF copper nanocomposites retain 90% of the initial strength to temperatures as high as 1173 K (or 0.87T_m, where T_m is the melting point of copper), which is better than the immiscible copper–niobium alloy (one of the most thermally stable copper alloys). The combination of high strength and high conductivity (Supplementary Fig. 12b) rivals Cu-Ag alloys, which are believed to have the best combination of strength and conductivity among all copper alloys but usually have low thermal stability. This synergy of excellent mechanical and functional properties in one material has prospective applications. For example, as-built strong yet ductile copper nanocomposites with high fatigue and thermal resistance properties are highly sought after for combustion chambers in rocket engines^{36–38}.

Discussion

Our study demonstrates an in situ nano-fragmentation and rapid-quenching mechanism for dispersions during L-PBF, by which densely populated amorphous nanoparticles can be deployed inside the metal matrix grains. These amorphous ceramic nanoparticles impose significant resistance to dislocation propagation, and at the same time absorb excess dislocations to avoid stress concentration. This, together with its self-hardening capability and thermal stability, renders the AM copper-based nanocomposites an unprecedented combination of mechanical and functional properties. This dispersion strategy is applicable to a variety of particle-metal systems, and particularly useful (or even indispensable) for those reflective metals (demonstrated above for Cu and Al) that are not amenable to L-PBF additive manufacturing. The idea of utilizing amorphous nanoparticles should also stimulate new designs when processing metals via other routes, such as powder metallurgy and chemical vapour deposition, where multiple options exist to tune the distributions and metastable states of the nanoparticles. We believe this innovative composite design strategy

can greatly expand the field of the microstructure engineering of metallic materials, towards unparalleled combination of properties for cutting-edge applications.

Methods

Materials fabrication

Gas-atomized copper powders with an average diameter of ~30 μm were mixed with highly crystallized B₄C particles with sizes ranging from 2 to 4 μm (Aladdin Ltd., Shanghai, China). The powder mixing was facilitated by using a high-shear dispersion facility (Nobilta, Hosokawa Micron Ltd., Japan) for 20 min at a rotation speed of 1600 rpm under the protection of argon. Composites were then built using a selective laser melting machine (S210, BLT, China) under high-purity argon to minimize oxidation (oxygen content: <50 ppm). This system was equipped with a single-mode fibre laser (500 W, 1064 nm wavelength) with a spot size of 60 μm. A cooling substrate system was designed in the printing machine to ensure a constant substrate temperature of -20 °C during L-PBF to ensure a high cooling rate upon sample building, and a continuous scanning strategy involving a 67° rotation before scanning another layer was adopted to randomize the crystal orientations and alleviate residual stresses in the built samples. The processing windows for high-density (>99.5%) metal nanocomposite samples were probed, and the key printing parameters are provided in Supplementary Table 1. Conventional high-strength copper was produced via cold rolling high-purity copper (70% thickness reduction), in which samples with grain sizes of ~400 nm were obtained. These samples were used for the comparison of mechanical properties in Fig. 3a.

We extracted nanoparticles from the composite made via L-PBF to enable a direct characterization of the nanoparticle structures. The as-built copper nanocomposites were etched in FeCl₃ solution acidized with hydrochloric acid, which allowed for the removal of the copper matrix. The residual nanoparticles were washed with deionized water three times, collected and dried at 60 °C for 24 h in a vacuum oven. For comparison, we annealed the as-built copper nanocomposites at 1173 K for 6 h to crystallize the B₄C nanoparticles. To minimize oxidation, the annealing process was conducted in a glove box with oxygen and water contents of less than 0.5 ppm.

Microstructural characterizations

XRD and NMR. The structures of the nanoparticles in the as-built copper nanocomposite were identified using XRD with a Cu target and an X-ray wavelength of 1.54059 Å on a D/Max-2500 instrument from Rigaku. Moreover, the chemical environments of the B atoms in the extracted nanoparticles were studied using ¹¹B NMR, in which the spectra were recorded at 14.1 T on a 600 MHz Bruker Avance Neo spectrometer. The spectrometer operated at ν_L = 160.5 MHz with a 4-mm Bruker probe and a spinning frequency of 14 kHz for the rotor. We acquired the spectra by using a spin-echo θ-τ-2θ pulse sequence (with θ = 90°). The spectra of the raw B₄C microparticles were obtained and compared under the same conditions.

NEXAFS. The atomic bonding structures of the extracted B₄C nanoparticles were probed using NEXAFS spectroscopy at the BL10B beamline of the National Synchrotron Radiation Laboratory, China. The B 1s NEXAFS spectra were recorded at room temperature under ultrahigh vacuum conditions of less than 10⁻⁸ Pa. The data were collected in total electron yield mode, with a rectangular beam size of 0.2 × 0.1 mm².

EBSD. A high-resolution EBSD system (Symmetry S2, Oxford) equipped with SEM (Scios, Thermo Fisher) was employed, with an angular resolution below 0.05°. AZtecCrystal and CorssCourt4 data processing software were used for EBSD data analysis. An accelerating voltage of 30 kV was used for EBSD data collection. Grain boundaries (GBs) with

misorientation angles of 2° – 10° and $>10^{\circ}$ were considered low- and high-angle GBs, respectively. EBSD samples were prepared using standard metallographic techniques, where the sample surface was finally polished with an ion-milling system (Model 1060, Fischione) to achieve a high validated hit rate ($>90\%$). For the quantitative strain/stress analyses of the deformed copper nanocomposite (with an applied strain of -3%), cross-correlation-based EBSD was conducted to measure the elastic strain fluctuation and local misorientation characteristics. The parameters of a long exposure time (1.5 s), zero gain and 1×1 binning were applied to collect high-quality Kikuchi patterns.

TEM. HRTEM was conducted at an operating voltage of 300 keV on a Thermo Fisher Spectra 300 transmission electron microscope equipped with an imaging aberration corrector. HAADF–STEM images with maximum point-to-point spatial resolutions of 0.05 nm were obtained with convergence angles of 26 mrad and collection semiangles ranging from 50 to 180 mrad. The elements were identified and their distributions were analysed in the nanoparticles using EDS (Bruker Super-X). TEM samples were prepared via the standard lift-out method using a focused ion beam (FIB) system. Further nanomilling (Nanomill 1040, Fischione) at 800 V was employed to remove the surface amorphous layer produced during FIB milling. PED-based ACOM was conducted via TEM at a step size of 1 nm.

APT. Atom probe tomography analyses were carried out in a CAMECA LEAP 4000 \times SI instrument under ultrahigh vacuum conditions of -2.5×10^{-11} Torr. The specimen temperature was 40 K, and the target evaporation rate was 0.5% per pulse under ultraviolet (UV) laser pulsing conditions with an energy of 40 pJ. APT specimens were prepared in a FIB system, where a very low accelerating voltage (5 kV) and beam current (5 pA) were employed in the final milling step to minimize Ga⁺ implantation. The CAMECA integrated visualization and analysis software IVAS 3.6.12 was used for data processing and three-dimensional atomic reconstruction.

Mechanical testing

Tensile and fatigue tests. Dog-bone specimens, each with a 10-mm gauge length, 2-mm width, and 1-mm thickness, were cut from AM-built copper nanocomposites and from conventional high-strength copper by electrodischarge machining (EDM). The tensile direction was perpendicular to the build direction for the printed samples, and was aligned with the rolling direction for grain-refined pure copper. The surfaces and sides of the tensile samples were polished with 360–4000-grit European metallographic silicon carbide papers, followed by polishing in 3- μ m and 1- μ m diamond suspensions. The final thicknesses of the tensile specimens were ~ 0.9 mm. Quasistatic uniaxial tensile tests were conducted in a universal testing machine (Instron 3344) at a constant strain rate of 5×10^{-4} s⁻¹. At least five tensile tests were carried out to obtain statistically meaningful values. Tensile elongation was measured using a static axial clip-on extensometer (Model 2630-101, Instron) with a 1- μ m displacement resolution. The fatigue test specimens were machined according to the American Society for Testing and Materials E466-21 standard for a pull–pull fatigue test with $R=0.1$. The specimens for fatigue testing were polished following the same procedures used for the tensile tests, and the fatigue tests were conducted with a high-frequency fatigue testing machine (Care M-6000, Tianjin, China) at a frequency of 15 Hz (sinusoidal wave).

Multiple stress relaxation tests. Multi-cycle relaxation was performed on Cu-8%-ANP nanocomposite at the specific engineering strain values of 1%, 2%, 3% and 4%, from which the evolution of physical activation volume as a function of applied strain can be deduced³⁹. The specimens underwent tensile testing at a strain rate of 5×10^{-4} s⁻¹ until the preset strain was reached, at which point the frame stopped, followed

by a holding time of 90 seconds. The stresses decreased during the relaxation period due to the continued glide of mobile dislocations. At the end of each relaxation cycle, the specimen was reloaded to the stress level before stress relaxation at a constant rate (50 N/s). Four relaxation cycles were conducted for each preset strain, allowing for the determination of the evolution of physical activation volume and the mobile dislocation exhaustion rate. The details of the calculation process can be found in our previous work³⁹.

In situ synchrotron X-ray diffraction experiment. In situ synchrotron X-ray diffraction (SXRD) tensile tests were conducted at beamline ID-3A, the Cornell High Energy Synchrotron Source, using an acceleration voltage of 52 keV. A dog-bone-shaped tensile specimen with nominal gauge dimensions of 2 mm (length) \times 1.2 mm (width) \times 1 mm (thickness) was loaded at a constant strain rate of 5×10^{-4} s⁻¹. Specimens for synchrotron-diffraction tensile tests were prepared following the same procedures as those for the tensile tests mentioned above. With a slit size of 0.5 mm (length) \times 2 mm (width), two-dimensional (2D) XRD patterns were collected in transmission mode at the gauge section of the tensile specimen with a DEXELA flat panel detector positioned 600 mm behind the sample. Single-peak fitting was performed by using GSAS-II software. The lattice strain for the $\{hkl\}$ reflection, ϵ_{hkl} , was calculated by $\epsilon_{hkl} = (d_{hkl} - d_{0,hkl})/d_{0,hkl}$, where d_{hkl} and $d_{0,hkl}$ denote the interplanar spacings of the $\{hkl\}$ planes under loading and in the stress-free state, respectively.

Computational modelling

Mesoscale powder bed fusion simulation. An unresolved computational fluid dynamics (CFD) and discrete element method (DEM) coupling model was applied to elucidate the laser powder bed fusion process of mixed copper and B₄C powders⁴⁰. The copper powder layer was generated by modelling the powder spreading process (i.e., a rake being pushed over a powder bed)⁴¹. The B₄C particles were randomly dispersed in the copper powder layer, where the volume fraction and powder diameter distribution were identical to those in the experimental setup. The mesoscale simulation applied a structural Eulerian mesh in the computational domain, and the finite volume method was employed to solve the governing fluid equations. A mesh size of 5 μ m was adopted to balance the accuracy and efficiency. The size of the computational domain was $2 \times 0.5 \times 0.5$ mm³. In the present work, the vapour flow and the resultant powder spattering were not included for simplification. The thermophysical properties (and the temperature-dependent thermophysical parameters) of copper and B₄C are listed in Supplementary Tables 2–4. Additional details of our modelling framework can be found in the Supplementary Materials.

Multiphysics modelling of droplet dispersion. A microscale model was developed to reveal the details of the fragmentation of B₄C from micro-sized to nano-sized droplets in the melt pool. A two-fluid CFD model with a sharp interface identification technique was applied to reveal the dispersion of microscale B₄C in the copper matrix. In this model, copper and B₄C were treated as fluid 1 and fluid 2, respectively. The governing equations of the two-fluid model were similar to those of the mesoscale CFD model, except that F in the VoF equation represented the volume fraction of fluid 1. In the present work, the van der Waals forces between different B₄C particles were not incorporated into the simulation since the van der Waals force was not significant compared with the hydraulic force exerted on the particle, even when the particle diameter was less than 10 nm^{12,42}.

In the present work, we chose a representative elementary volume (REV; with a size of $5.0 \times 5.0 \times 5.0$ μ m³) from the mesoscale simulation domain as the simulation domain of the microscale model. The temperature and velocity histories of the REV from the mesoscale simulation were then extracted and set as the flow pattern (e.g., temperature and average velocity of fluid) of the microscale

simulation. The mesh size was set to 0.025 μm to balance the accuracy and efficiency of the microscale simulation. During the dispersion process, if the B_4C fluid was dispersed into a submesh isolated droplet (i.e., the volume of the B_4C droplet was smaller than the mesh cell volume), the submesh isolated droplet was replaced with a DEM particle, where the mass, momentum and energy of the DEM particle were identical to those of B_4C . After the solidification of copper, we calculated the number and volume of isolated B_4C droplets in the domain. For the counting of submesh isolated droplets, if the distance between the centres of two particles d_{12} was smaller than the summation of their radii ($r_1 + r_2$), the two particles were treated as one droplet with a volume equal to the summation of these two isolated droplets.

Laser absorptivity modelling. We developed a ray-tracing simulation to assess laser absorption in mixed powder beds, including two different powders: copper (40 μm in diameter) and B_4C (5 μm in diameter). For copper particles, we utilized geometric optics to model reflection, enabling us to trace ray propagation and calculate energy absorption based on incidence angles and reflection properties of copper. In contrast, scattering of laser beam was considered in the simulation of B_4C particles due to their small size. This method allowed us to capture the intricate interactions between the laser and the mixed powder beds, and to identify the absorbed laser energy for copper and B_4C microparticles, respectively.

MD simulation. Molecular dynamics simulations were performed using large-scale atomic/molecular massively parallel simulator⁴³ software to examine the interactions between dislocations and B_4C nanoparticles during deformation. The Cu–Cu interaction was described by the embedded atom method potential⁴⁴. The Stillinger–Weber (SW) potential was adopted for B–B, C–C and B–C interactions⁴⁵. The Lennard–Jones potential was used for Cu–B^{46,47} and Cu–C interactions⁴⁸. The radii of the ANPs and CNPs were set to 3 nm, and the particles were embedded in a copper matrix with preexisting edge dislocations of $\mathbf{b} = a_0/2 [10\bar{1}]$ on the $\{111\}$ plane. Crystalline B_4C with a C–B–C chain was chosen for the structures of the CNPs. ANP was generated by packing B_{11}C clusters and C–B–C chains and relaxed using the SW potential⁴⁵. The simulation cell was oriented with the X, Y and Z directions aligning along the $[10\bar{1}]$, $[1\bar{2}1]$, and $[111]$ directions of the copper matrix. The simulation cells were 38.2, 22.1 and 25.0 nm in length along the X, Y and Z directions, respectively, with ~ 1.7 million atoms. The time step in the simulation was 2 fs. After the B_4C nanoparticles were embedded in the copper matrix, the simulation cell was optimized using the conjugate gradient method and subsequently held at 10 K for 30,000 steps. Then, the upper and lower regions with thicknesses of 5 atomic layers were selected and moved along the positive and negative X directions, respectively, at a fixed velocity. The rate of applied shear strain was 10^7 s^{-1} . The open visualization tool package⁴⁹ was adopted to produce the von Mises equivalent atomic strain map and visualize the atomic structures, as shown in Fig. 4e, f.

Moreover, the structures of the ANP generated by different methods were analysed via MD simulations. Following previous work⁴⁵, B_{11}C units and C–B–C chains were randomly packed using packmol⁵⁰, and the structures were annealed at 300 K and optimized by minimizing the potential energy (PE). The amorphous B_4C structure was cut into spheres and embedded into a Cu matrix to obtain the Cu–ANP atomic model. Alternatively, crystalline B_4C particles with radii of 3 nm were embedded into a Cu matrix. Then, the temperatures of the B_4C particles were all increased to 3500 K for 0.5 ns, while the temperature of the matrix was maintained at 300 K. Different temperatures were used for the particles and the matrix to avoid melting the Cu matrix (hence, the formation of solidification defects upon cooling). Afterwards, the simulation cell was optimized to obtain the ANP/Cu atomic model. The alternative modelling process showed similar atomic deformation mechanisms. Specifically, the potential energies of the

ANPs generated by packmol or by the melting of B_4C CNPs both decreased as shearing strain was applied. Different melting times (0.3 ns vs. 0.5 ns) led to the presence of distinct amorphous particles, but for both cases, the potential energies of the B_4C particles decreased during shearing loading. Therefore, the ability to accommodate the shearing strain originated from the ANPs, irrespective of the method used to construct the ANP/Cu atomic model. To analyse the changes in the ANPs during deformation, every 10,000 atomic structures during shearing were optimized to produce a stress-free state, and the PEs of the stress-free ANPs were subsequently calculated. The stress-free state was obtained by minimizing the PE of the whole cell; the largest components of forces on any atoms were lower than $10^{-15} \text{ eV}/\text{\AA}$. The PEs of the stress-free ANPs generated by the random packing of B_{11}C units and C–B–C chains are shown as a function of the applied shear strain in Fig. 4g.

CPFE simulations. A dual-phase crystal plasticity model was developed to understand the lattice strain changes in in situ synchrotron–diffraction experiments. We used the rate-dependent finite strain crystal plasticity constitutive model for the copper matrices and the rate-independent finite strain J2 plasticity model for the CNPs/ANPs. We simulated the uniaxial tension of copper nanocomposites containing 12 vol.% B_4C nanoparticles at a strain rate of 10^{-4} s^{-1} .

For the copper matrix, the deformation gradient in each grain \mathbf{F} was decomposed into $\mathbf{F} = \mathbf{F}^e \mathbf{F}^p$, where \mathbf{F}^e is the elastic deformation gradient and \mathbf{F}^p is the plastic deformation gradient. Then, the elastic Green strain tensor was calculated as $\mathbf{E}^e = 1/2(\mathbf{F}^{eT} \mathbf{F}^e - \mathbf{I})$, and the second Piola–Kirchhoff stress \mathbf{T} in the intermediate configuration was determined as $\mathbf{T} = \mathbf{C} : \mathbf{E}^e$, where \mathbf{I} is the second-order identity tensor and \mathbf{C} is the fourth-order elastic tensor of a single crystal Cu. The change in the plastic deformation gradient was determined by the plastic velocity gradient:

$$\dot{\mathbf{F}}^p = \mathbf{L}^p \mathbf{F}^p \text{ and } \mathbf{L}^p = \sum_{i=1}^{12} \dot{\gamma}_i^p \mathbf{m}_i \otimes \mathbf{n}_i \quad (1)$$

where $\dot{\gamma}_i^p$ is the plastic shearing rate on the i -th slip system and \mathbf{m}_i and \mathbf{n}_i are the associated slip direction and slip plane normal, respectively. Twelve $\{111\} \langle 110 \rangle$ slip systems were considered for the FCC copper phase. The plastic shearing rate $\dot{\gamma}_i^p$ was determined to follow a power law relationship:

$$\dot{\gamma}_i^p = \dot{\gamma}_0^p |\tau_i / s_i|^{1/m} \text{sgn}(\tau_i) \quad (2)$$

where $\dot{\gamma}_0^p$ is the reference shear rate, $\tau_i = \mathbf{m}_i \cdot \mathbf{T} \cdot \mathbf{n}_i$ is the resolved shear stress, m is the rate sensitivity and s_i is the slip resistance of the i -th slip system. The slip resistance of each slip system began with an identical initial value s_0 and hardened according to $\dot{s}_i = \sum_j h_{ij} |\dot{\gamma}_j^p|$. The hardening matrix was expressed as follows:

$$h_{ij} = q_{ij} h_0 \left(1 - s_j / s_{\text{sat}}\right)^a \quad (3)$$

where the latent hardening matrix q_{ij} is equal to 1.0 and the off-diagonal elements are equal to 1.4.

For the B_4C nanoparticles, the isotropic hardening plasticity model was adopted. The constitutive equation was formulated in a corotational framework based on the Jaumann stress rate. The Jaumann rate of stress was determined by the following equation:

$$\dot{\boldsymbol{\sigma}}^J = \mathbf{C} : \dot{\boldsymbol{\varepsilon}}^e \quad (4)$$

where \mathbf{C} is the elastic tensor of the boron carbide nanoparticles calculated from the Young's modulus E_{NP} and Poisson's ratio ν_{NP} . The

rate-independent yield function was as follows:

$$\sqrt{\frac{3}{2} S_{ij} S_{ij}} - \sigma_y (\bar{\epsilon}^{pl}) = 0 \quad (5)$$

where $S_{ij} = \sigma_{ij} - \frac{1}{3} \delta_{ij} \sigma_{kk}$ is the deviatoric stress and $\bar{\epsilon}^{pl} = \int_0^t \dot{\epsilon}^{pl} dt$ is the equivalent plastic strain with $\dot{\epsilon}^{pl} = \sqrt{\frac{2}{3} \dot{\epsilon}_{ij}^{pl} \dot{\epsilon}_{ij}^{pl}}$. The plastic flow law determined the plastic strain rate, $\dot{\epsilon}_{ij}^{pl} = \frac{3}{2} \frac{S_{ij}}{\sigma_y} \dot{\epsilon}^{pl}$. The yield strength was assumed to be linear isotropic hardening, $\sigma_y = \sigma_y^0 + h_{NP} \bar{\epsilon}^{pl}$. The radial return scheme was applied to determine the plastic strain increment. The dual-phase crystal plasticity model was solved using the vectorized user material (VUMAT) subroutine in Abaqus/Explicit. The parameters used in the above constitutive model are listed in Supplementary Table 5.

Electrical conductivity and thermal stability measurements

The electrical conductivities of the AM-based copper nanocomposites were measured by an eddy current conductivity meter at room temperature, and the values are expressed in terms of the International Annealed Copper Standard. High-purity annealed copper was used for calibration purposes. All samples used for electrical conductivity measurements were polished to a metallurgical grit of 4000 with SiC paper. The as-built copper nanocomposites were annealed at different temperatures (from 673 K to 1173 K) for 1 h to evaluate their thermal stabilities. Annealing was performed in an argon environment, and the Vickers hardness was measured under a load of 294.2 N for 10 s. The annealing temperature–strength (hardness) retention curve, as shown in Fig. 3e, was plotted because the strength of a material was proportional to its hardness⁵¹.

Estimating the yield strength of the as-built nanocomposites

We estimated the yield strength of the Cu-12%-ANP nanocomposite by considering the contributions from grain refinement, dislocations and nanoparticle-induced strengthening. The contribution of the Orowan strengthening ($\Delta\sigma_{\text{Orowan}}$) mechanism induced by well-dispersed particles was calculated by the following equation⁵²:

$$\Delta\sigma_{\text{Orowan}} = \frac{\varphi G b}{d_p} \left(\frac{6f}{\pi} \right)^{1/3} \quad (6)$$

where G , b , f and d_p are the shear modulus of the matrix, the magnitude of the Burgers vector, the volume fraction and the average size of the nanoparticles, respectively. φ is a constant equal to 2⁵². Considering that in this study $G_m = 47.7$ GPa, $b = 0.256$ nm, $V_p = 0.12$ and $d_p = 82.6$ nm, the calculated $\Delta\sigma_{\text{Orowan}}$ was 318 MPa. We estimated the dislocation density (ρ) in our as-built Cu-12%-ANP to be $(2.3 \pm 0.3) \times 10^{14} \text{ m}^{-2}$ according to the modified Williamson–Hall method^{53,54}. Their contribution to yield stress ($\Delta\sigma_{\text{Dis}}$) was estimated from the classical Taylor relationship:

$$\Delta\sigma_{\text{Dis}} = \alpha M G b \rho^{0.5} \quad (7)$$

where α is a geometrical factor ($\sim 0.2^3$) and M is the Taylor factor (~ 3.06 for FCC metals containing weak textures³). Therefore, the strengthening contribution from dislocations was 115.8 MPa in Cu-12%-ANP. The yield strength from the Hall–Petch effect ($\Delta\sigma_{\text{HP}}$) was estimated by the following equations as a result of the grain refinement⁵⁵:

$$\Delta\sigma_{\text{HP}} = \sigma_0 + k D^{-1/2} \quad (8)$$

where D is the grain size (~ 390 nm), k is a constant ($0.14 \text{ MPa}\cdot\text{m}^{1/2}$), and σ_0 is the lattice friction stress and is $\sim 25 \text{ MPa}$ ⁵⁵. $\Delta\sigma_{\text{HP}}$ is then calculated

to be 249.2 MPa. Therefore, the high yield strength of our as-built Cu-12%-ANP (~ 730 MPa) is mainly contributed by the Orowan strengthening of densely distributed nanoparticles and further enhanced by the high densities of dislocations and grain refinement after performing L-PBF.

Reporting summary

Further information on research design is available in the Nature Portfolio Reporting Summary linked to this article.

Data availability

The data that support the findings of this study are available within the main text and the Supplementary Information file. Due to the interdisciplinary nature of the study and the large volume of data, additional data supporting the findings are available from the corresponding author upon request.

References

- Kim, S. H., Kim, H. & Kim, N. J. Brittle intermetallic compound makes ultrastrong low-density steel with large ductility. *Nature* **518**, 77–79 (2015).
- Gao, J. et al. Facile route to bulk ultrafine-grain steels for high strength and ductility. *Nature* **590**, 262–267 (2021).
- Chen, L. Y. et al. Processing and properties of magnesium containing a dense uniform dispersion of nanoparticles. *Nature* **528**, 539–543 (2015).
- Hu, Y. & Curtin, W. A. Modeling of precipitate strengthening with near-chemical accuracy: case study of Al-6xxx alloys. *Acta Mater.* **237**, 118144 (2022).
- Weertman, J. *Dislocation Based Fracture Mechanics*. (WORLD SCIENTIFIC, 1996).
- Peng, S., Wei, Y. & Gao, H. Nanoscale precipitates as sustainable dislocation sources for enhanced ductility and high strength. *Proc. Natl. Acad. Sci. USA* **117**, 5204–5209 (2020).
- Wang, Y., Li, J., Hamza, A. V. & Barbee, T. W. Jr Ductile crystalline-amorphous nanolaminates. *Proc. Natl. Acad. Sci. USA* **104**, 11155–11160 (2007).
- Khalajhedayati, A., Pan, Z. & Rupert, T. J. Manipulating the interfacial structure of nanomaterials to achieve a unique combination of strength and ductility. *Nat. Commun.* **7**, 10802 (2016).
- Kotadia, H. R., Gibbon, G., Das, A. & Howes, P. D. A review of laser powder bed fusion additive manufacturing of aluminium alloys: microstructure and properties. *Addit. Manuf.* **46**, 102155 (2021).
- Zhang, T. et al. In situ design of advanced titanium alloy with concentration modulations by additive manufacturing. *Science* **374**, 478–482 (2021).
- Ren, J. et al. Strong yet ductile nanolamellar high-entropy alloys by additive manufacturing. *Nature* **608**, 62–68 (2022).
- Wang, G. et al. Enhanced plasticity due to melt pool flow induced uniform dispersion of reinforcing particles in additively manufactured metallic composites. *Int. J. Plast.* **164**, 103591 (2023).
- Liu, Y. et al. Manufacturing of high strength and high conductivity copper with laser powder bed fusion. *Nat. Commun.* **15**, 1283 (2024).
- Pallier, C. et al. Structure of an amorphous boron carbide film: an experimental and computational approach. *Chem. Mater.* **25**, 2618–2629 (2013).
- Mc Ilroy, D. N. et al. Electronic and dynamic studies of boron carbide nanowires. *Phys. Rev. B Condens. Matter Mater. Phys.* **60**, 4874–4879 (1999).
- Monteiro, O. R., Delplancke-Ogletree, M. P. & Klepper, C. C. Boron carbide coatings prepared by cathodic arc deposition. *J. Mater. Sci.* **38**, 3117–3120 (2003).

17. Jadhav, S. D., Goossens, L. R., Kinds, Y., Van Hooreweder, B. & Vanmeensel, K. Laser-based powder bed fusion additive manufacturing of pure copper. *Addit. Manuf.* **42**, 101990 (2021).
18. Qu, S. et al. High-precision laser powder bed fusion processing of pure copper. *Addit. Manuf.* **48**, 102417 (2021).
19. Khairallah, S. A. et al. Controlling interdependent meso-nanosecond dynamics and defect generation in metal 3D printing. *Science* **368**, 660–665 (2020).
20. Qu, M. et al. Controlling process instability for defect lean metal additive manufacturing. *Nat. Commun.* **13**, 1079 (2022).
21. Qu, M. et al. Nanoparticle-enabled increase of energy efficiency during laser metal additive manufacturing. *Addit. Manuf.* **60**, 103242 (2022).
22. Liu, G. et al. Nanostructured high-strength molybdenum alloys with unprecedented tensile ductility. *Nat. Mater.* **12**, 344–350 (2013).
23. Kim, C. T., Lee, J. K. & Plichta, M. R. Plastic relaxation of thermo-elastic stress in aluminum/ceramic composites. *Metall. Trans. A* **21**, 673–682 (1990).
24. Ma, E. & Zhu, T. Towards strength-ductility synergy through the design of heterogeneous nanostructures in metals. *Mater. Today* **20**, 323–331 (2017).
25. Kumar, G., Neibecker, P., Liu, Y. H. & Schroers, J. Critical fictive temperature for plasticity in metallic glasses. *Nat. Commun.* **4**, 1536 (2013).
26. Brandl, C., Germann, T. C. & Misra, A. Structure and shear deformation of metallic crystalline-amorphous interfaces. *Acta Mater.* **61**, 3600–3611 (2013).
27. Cheng, B. & Trelewicz, J. R. Mechanistic coupling of dislocation and shear transformation zone plasticity in crystalline-amorphous nanolaminates. *Acta Mater.* **117**, 293–305 (2016).
28. Chen, Y. et al. The origin of exceptionally large ductility in molybdenum alloys dispersed with irregular-shaped La_2O_3 nanoparticles. *Nat. Commun.* **15**, 4105 (2024).
29. Pan, J., Ivanov, Y. P., Zhou, W. H., Li, Y. & Greer, A. L. Strain-hardening and suppression of shear-banding in rejuvenated bulk metallic glass. *Nature* **578**, 559–562 (2020).
30. Wu, G., Chan, K. C., Zhu, L., Sun, L. & Lu, J. Dual-phase nanostructuring as a route to high-strength magnesium alloys. *Nature* **545**, 80–83 (2017).
31. Ming, K. et al. Enhancing strength and ductility via crystalline-amorphous nanoarchitectures in TiZr-based alloys. *Sci. Adv.* **8**, eabm2884 (2022).
32. Antolovich, S. D. & Armstrong, R. W. Plastic strain localization in metals: origins and consequences. *Prog. Mater. Sci.* **59**, 1–160 (2014).
33. Long, J. et al. Improved fatigue resistance of gradient nanograined Cu. *Acta Mater.* **166**, 56–66 (2019).
34. Deschamps, A. & Hutchinson, C. R. Precipitation kinetics in metallic alloys: experiments and modeling. *Acta Mater.* **220**, 117338 (2021).
35. Philippe, T. & Voorhees, P. W. Ostwald ripening in multicomponent alloys. *Acta Mater.* **61**, 4237–4244 (2013).
36. Blachowicz, T., Ehrmann, G. & Ehrmann, A. Metal additive manufacturing for satellites and rockets. *Appl. Sci.* **11**, 12036 (2021).
37. Gradl, P. et al. Advancement of extreme environment additively manufactured alloys for next generation space propulsion applications. *Acta Astronaut.* **211**, 483–497 (2023).
38. Morshed-Behbahani, K., Aliyu, A., Bishop, D. P. & Nasiri, A. Additive manufacturing of copper-based alloys for high-temperature aerospace applications: a review. *Mater. Today Commun.* **38**, 108395 (2024).
39. Li, Z., Li, Z. Q., Tan, Z., Xiong, D. B. & Guo, Q. Stress relaxation and the cellular structure-dependence of plastic deformation in additively manufactured AlSiOMg alloys. *Int. J. Plast.* **127**, 102640 (2020).
40. Norouzi, H. R., Zarghami, R., Sotudeh-Gharebagh, R. & Mostoufi, N. *Coupled CFD-DEM Modeling: Formulation, Implementation and Application to Multiphase Flows*. (John Wiley & Sons, Inc., 2016).
41. Chen, H. et al. Powder-spreading mechanisms in powder-bed-based additive manufacturing: experiments and computational modeling. *Acta Mater.* **179**, 158–171 (2019).
42. Zhang, Y. et al. Dispersion of reinforcing micro-particles in the powder bed fusion additive manufacturing of metal matrix composites. *Acta Mater.* **235**, 118086 (2022).
43. Plimpton, S. Fast parallel algorithms for short-range molecular dynamics. *J. Comput. Phys.* **117**, 1–19 (1995).
44. Mishin, Y., Mehl, M. J., Papaconstantopoulos, D. A., Voter, A. F. & Kress, J. D. Structural stability and lattice defects in copper: ab initio, tight-binding, and embedded-atom calculations. *Phys. Rev. B Condens. Matter Mater. Phys.* **63**, 2241061–22410616 (2001).
45. Khadka, R., Baishnab, N., Opletal, G. & Sakidja, R. Study of amorphous boron carbide (a-B₂C) materials using molecular dynamics (MD) and hybrid reverse monte carlo (HRMC). *J. Non Cryst. Solids* **530**, 119783 (2020).
46. Filippova, V. P., Kunavin, S. A. & Pugachev, M. S. Calculation of the parameters of the Lennard-Jones potential for pairs of identical atoms based on the properties of solid substances. *Inorg. Mater. Appl. Res.* **6**, 1–4 (2015).
47. Mayo, S. L., Olafson, B. D. & Goddard Iii, W. A. DREIDING: a generic force field for molecular simulations. *J. Phys. Chem.* **94**, 8897–8909 (1990).
48. Guo, Y. & Guo, W. Structural transformation of partially confined copper nanowires inside defected carbon nanotubes. *Nanotechnology* **17**, 4726–4730 (2006).
49. Stukowski, A. Visualization and analysis of atomistic simulation data with OVITO—the open visualization tool. *Model. Simul. Mater. Sci. Eng.* **18**, 015012 (2010).
50. Martínez, L., Andrade, R., Brigin, E. G. & Martínez, J. M. PACKMOL: a package for building initial configurations for molecular dynamics simulations. *J. Comput. Chem.* **30**, 2157–2164 (2009).
51. Zhang, P., Li, S. X. & Zhang, Z. F. General relationship between strength and hardness. *Mater. Sci. Eng. A* **529**, 62–73 (2011).
52. Zeng, W. et al. Bulk Cu-NbC nanocomposites with high strength and high electrical conductivity. *J. Alloy. Compd.* **745**, 55–62 (2018).
53. Williamson, G. K. & Hall, W. H. X-ray line broadening from filed aluminium and wolfram. *Acta Met.* **1**, 22–31 (1953).
54. Ungár, T. & Borbély, A. The effect of dislocation contrast on x-ray line broadening: a new approach to line profile analysis. *Appl. Phys. Lett.* **69**, 3173–3175 (1996).
55. Hansen, N. Hall-Petch relation and boundary strengthening. *Scr. Mater.* **51**, 801–806 (2004).

Acknowledgements

D.Z. and Z.L. acknowledge support from the National Natural Science Foundation of China (Grant Nos. 52171142 and 52192595), and Shanghai Jiao Tong University 2030 Initiative. Y.Z. and W.Y. acknowledge support from the Ministry of Education, Singapore, under its Academic Research Fund Tier 2 (MOET2EP50121-0017). E.M. acknowledges support from National Natural Science Foundation of China (Grant No. 52231001).

Author contributions

Z.L. and E.M. guided the research tasks. G.W. and B.Z. fabricated the samples and carried out the mechanical testing/microstructural analysis. Y.Z., T.Z., Y.M.Z., Z.H., L.W., W.Y., K.W. and J.D. performed the modelling. B.C., Q.O. conducted the TEM analysis and fatigue data acquisition. S.J. conducted the APT experiment and analysis. J.L., W.C. and Y.M.W. designed and performed the in situ synchrotron X-ray tensile experiments. Z.L., W.C., D.Z. and E.M. wrote the paper. All authors participated in the discussion, review and editing of the manuscript.

Competing interests

The authors declare no competing interests.

Additional information

Supplementary information The online version contains supplementary material available at <https://doi.org/10.1038/s41467-025-58893-1>.

Correspondence and requests for materials should be addressed to Zan Li, Di Zhang or Evan Ma.

Peer review information *Nature Communications* thanks Thomas Par-doen and the other, anonymous, reviewer(s) for their contribution to the peer review of this work. A peer review file is available.

Reprints and permissions information is available at <http://www.nature.com/reprints>

Publisher's note Springer Nature remains neutral with regard to jurisdictional claims in published maps and institutional affiliations.

Open Access This article is licensed under a Creative Commons Attribution-NonCommercial-NoDerivatives 4.0 International License, which permits any non-commercial use, sharing, distribution and reproduction in any medium or format, as long as you give appropriate credit to the original author(s) and the source, provide a link to the Creative Commons licence, and indicate if you modified the licensed material. You do not have permission under this licence to share adapted material derived from this article or parts of it. The images or other third party material in this article are included in the article's Creative Commons licence, unless indicated otherwise in a credit line to the material. If material is not included in the article's Creative Commons licence and your intended use is not permitted by statutory regulation or exceeds the permitted use, you will need to obtain permission directly from the copyright holder. To view a copy of this licence, visit <http://creativecommons.org/licenses/by-nc-nd/4.0/>.

© The Author(s) 2025